



Deposited via The University of Leeds.

White Rose Research Online URL for this paper:

<https://eprints.whiterose.ac.uk/id/eprint/179053/>

Version: Accepted Version

---

**Article:**

Xu, Z, Seddon, JM, Beales, P et al. (2021) Breaking Isolation to Form New Networks: pH-Triggered Changes in Connectivity Inside Lipid Nanoparticles. *Journal of the American Chemical Society*. ISSN: 0002-7863

<https://doi.org/10.1021/jacs.1c06244>

---

© 2021 American Chemical Society. This is an author produced version of an article published in *Journal of the American Chemical Society (JACS)*. Uploaded in accordance with the publisher's self-archiving policy.

**Reuse**

Items deposited in White Rose Research Online are protected by copyright, with all rights reserved unless indicated otherwise. They may be downloaded and/or printed for private study, or other acts as permitted by national copyright laws. The publisher or other rights holders may allow further reproduction and re-use of the full text version. This is indicated by the licence information on the White Rose Research Online record for the item.

**Takedown**

If you consider content in White Rose Research Online to be in breach of UK law, please notify us by emailing [eprints@whiterose.ac.uk](mailto:eprints@whiterose.ac.uk) including the URL of the record and the reason for the withdrawal request.



20 **ABSTRACT**

21 There is a growing demand to develop smart nanomaterials that are structure-responsive as they  
22 have the potential to offer enhanced dose, temporal and spatial control of compounds and chemical  
23 processes. The naturally occurring pH gradients found throughout the body make pH an attractive  
24 stimulus for guiding the response of a nanocarrier to specific locations or (sub)cellular  
25 compartments in the body. Here we have engineered highly sensitive lyotropic liquid crystalline  
26 nanoparticles that reversibly respond to changes in pH by altering the connectivity within their  
27 structure at physiological temperatures. At pH 7.4, the nanoparticles have an internal structure  
28 consisting of discontinuous inverse micellar ‘aqueous pockets’ based on space group Fd3m. When  
29 the pH is  $\leq 6$ , the nanoparticles change from a compartmentalized to an accessible porous internal  
30 structure based on a 2D inverse hexagonal phase (plane group p6mm). We validate the internal  
31 symmetry of the nanoparticles using Small Angle X-ray Scattering and cryogenic Transmission  
32 Electron Microscopy. The high resolution electron microscopy images obtained have allowed us  
33 for the first time to directly visualize the internal structure of the Fd3m nanoparticles and resolve  
34 the two different-sized inverse micelles that make up the structural motif within the Fd3m unit  
35 cell, which upon structural analysis reveal excellent agreement with theoretical geometrical  
36 models.

37

38

39

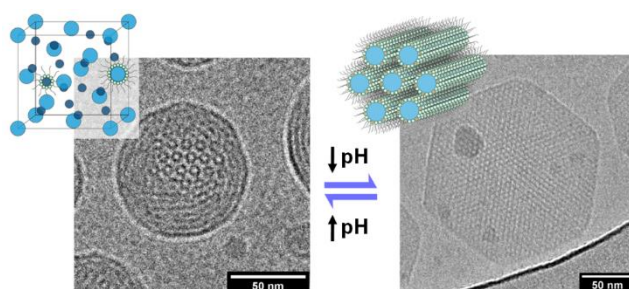
40

41

42

43

44 **TOC**



45

46

## 47 **INTRODUCTION**

48 Lyotropic liquid crystalline nanoparticles (LCNPs) have attracted enormous interest for  
49 applications such as drug delivery, nanoreactor arrays, biosensors, templating, advanced  
50 biomaterials and functional foods. These particles have non-lamellar internal nanostructures that  
51 possess two- or three-dimensional periodicity. LCNPs with internal nanostructures based on  
52 inverse bicontinuous cubics ( $Q_{II}$ ), 2D-hexagonal ( $H_{II}$ ) or ordered micellar phases are termed  
53 cubosomes, hexosomes and micellosomes respectively. They offer potential advantages over  
54 current nanoformulations, including favourable payloads due to their high internal surface area,  
55 simple preparation protocols, superior ease of conjugation with target biomolecules,  
56 biodegradability of the host building blocks and the ability to encapsulate hydrophobic,  
57 hydrophilic and amphiphilic substances.<sup>1-6</sup>

58 Currently there is a large demand to develop smart nanocarriers that can respond to particular  
59 environmental stimuli which could be used to release an active at a specific site of action and hence  
60 minimize off target toxicity and unwanted side effects. Extrinsic factors such as ultrasound,  
61 temperature, magnetic fields and light have been explored to trigger a response however these can  
62 only be controlled via external sources.<sup>7</sup> On the contrary, one can harness intrinsic stimuli such as

63 enzymes overexpressed at disease sites or variations in pH throughout the body, such as that found  
64 in the stomach, or the more acidic extracellular microenvironment of tumor cells compared to  
65 healthy tissue.<sup>8-10</sup> Acidic environments are also present in other organs/organelles such as the skin  
66 surface where the pH is around 4-6.5,<sup>11</sup> <4 in the gastric phase,<sup>12</sup> and between 4.5-6.5 in the  
67 lysosomal and endosomal lumen,<sup>13</sup> while the pH in the serum is 7.4. Acidic pH is also used *in vivo*  
68 to trigger processes such as protein-ligand binding and viral fusion.<sup>14</sup>

69  
70 Whilst the majority of pH responsive systems have been focused on polymers,<sup>15-16</sup> LCNPs are  
71 mainly made up of biological amphiphiles rendering them more biocompatible and less cytotoxic.<sup>6,</sup>  
72 <sup>17-18</sup> Non-lamellar forming lipids are some of the most common building blocks to generate inverse  
73 lyotropic liquid crystalline phases as they can form a variety of structures depending on  
74 composition, thermodynamic variables, pH and other parameters.<sup>19-21</sup> The resulting phase behavior  
75 is also dependent on the geometric packing of the lipids and can be tuned by increasing the  
76 concentration of more strongly curved lipids which will increase the negative spontaneous  
77 curvature towards the water and form phases with increasing negative interfacial curvature.  
78 **(Figure 1a)**. A full range of inverse lyotropic lipid phase transitions with increasing amphiphile  
79 concentration and increasing curvature can be seen in Kaasgaard and Drummond.<sup>22</sup> For example,  
80 by increasing the fatty acid content in monoolein (MO) based systems, the structure can transform  
81 from Q<sub>II</sub> to H<sub>II</sub> and on further addition to a discontinuous inverse micellar cubic phase of space  
82 group Fd3m.<sup>23-25</sup> In an analogous fashion, the phase behavior can be tuned by introducing ionisable  
83 lipids where the lipid headgroup can be protonated or deprotonated depending on the pH and ionic  
84 strength. An increase in surface charge density will cause electrostatic repulsion between  
85 headgroups, an increase of the effective headgroup area and consequently a decrease in the

86 magnitude of the spontaneous inverse curvature and the adoption of less curved phases (**Figure**  
87 **1a**). Similarly, an increase in ionic strength will enhance charge screening and hinder the transition  
88 to less curved structures. Tuning the phase behavior of these systems is attractive as the release  
89 rate of encapsulated actives from LCNPs strongly correlates with the internal nanostructure  
90 symmetry as well as, for some LCNPs, the geometry and dimensions of their pores.<sup>10, 26-27</sup>

91 Most studies have focused on pH-induced transitions between lamellar ( $L\alpha$ ) and  $Q_{II}$ , or between  
92  $Q_{II}$  and  $H_{II}$  phases. A MO: linoleic acid system was developed to change from  $Q_{II}$  at pH 7 to  $H_{II}$  at  
93 pH 2 to simulate intestinal and gastric phases respectively.<sup>28</sup> Negrini *et al.* further developed a  
94 monolinolein: pyridinylmethyl linoleate system that switched from an  $H_{II}$  to a  $Q_{II}$  phase when the  
95 pH was  $\leq 5.5$  and showed the potential therapeutic role of this targeted system in treating cancer  
96 cells by exploiting their more acidic microenvironment.<sup>29</sup> A low pH-induced  $L\alpha$  to  $Q_{II}$  phase  
97 transition in a MO: dioleoylphosphatidylserine system showed that the  $L\alpha$  phase directly  
98 transformed into an  $H_{II}$ , and subsequently, the  $H_{II}$  slowly converted into a  $Q_{II}$  phase.<sup>30</sup>

99 On the contrary, pH-triggered transitions from ordered inverse micellar phases is still in its  
100 infancy. These have an internal structure consisting of discontinuous micellar ‘pockets’ and, unlike  
101 the porous  $Q_{II}$  and  $H_{II}$  phases, these are based on a discontinuous packing of inverse micelles,  
102 containing an array of individual nanoscale aqueous compartments separated by fluid hydrophobic  
103 regions, which could potentially offer containment control.

104 Salentinig *et al.* showed that by increasing the pH from 6.8 to 9 at 25 °C in MO: oleic acid (OA)  
105 dispersions, an inverse micellar solution transformed to Fd3m micellosomes, to hexosomes, to  
106 cubosomes and finally to liposomes.<sup>31</sup> Similar phase transitions from LCNPs of OA doped with  
107 the antimicrobial human cathelicidin LL-37 peptide were observed upon increasing the pH from  
108 6 to 8 at 25 °C.<sup>32</sup> Recently Fong *et al.* showed that at a certain MO: fatty acid composition Fd3m

109 micellosomes were formed in water with a pH of 4.9 and very low ionic strength. When water was  
110 replaced by PBS (pH 7.4) the micellosomes transformed to hexosomes at 30 °C. This transition  
111 was however triggered by the combination of pH and ionic concentration changes, and thus cannot  
112 be considered a pure pH response.<sup>33</sup>

113 In this work we aim to develop LCNPs that are switchable between the confined Fd3m and  
114 porous H<sub>II</sub> phases at physiologically relevant temperature and pHs, confirmed with detailed  
115 structural characterization by SAXS and cryo-TEM. We designed pH-responsive LCNPs based on  
116 MO and oleyl alcohol (Olaic) doped with a small amount (3 mol%) of a pH-sensitive lipid. We  
117 show that these LCNPs transform from Fd3m micellosomes at pH 7.4 to hexosomes when the pH  
118 is  $\leq 6$ . To the best of our knowledge this is the first report of a pH triggered LCP transition from  
119 Fd3m micellosomes to hexosomes with decreasing pH and compared to previous research on  
120 similar transitions, our system can reversibly transform at both room (25 °C) and at a biologically-  
121 relevant temperature (37 °C). We highlight that high resolution cryo-TEM images have allowed  
122 us to directly visualize the internal structure of the Fd3m nanoparticles with unprecedented detail  
123 allowing us to compare the internal structures of the nanoparticles with theoretical predictions,  
124 using cryo-TEM for this purpose for the first time.

125

## 126 **RESULTS AND DISCUSSION**

127

### 128 **Phase behavior of oleyl alcohol, monoolein and DOBAQ mixtures reveal an H<sub>II</sub> to Fd3m** 129 **transition**

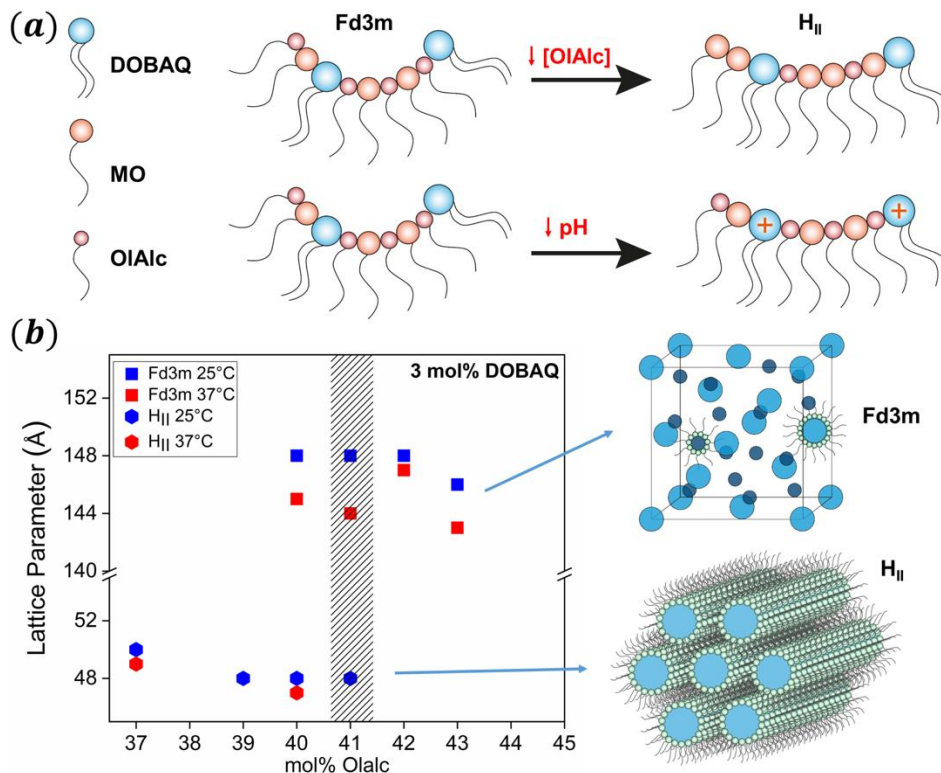
130 The phase diagram of MO in water has been widely studied;<sup>34-35</sup> above the excess water point of  
131 35 wt%, MO adopts a Pn3m bicontinuous cubic phase between approximately 20 and 80 °C, which  
132 then transforms to an inverse hexagonal (H<sub>II</sub>) phase at higher temperatures. Generally, for the other

133 pure component systems, DOBAQ forms liposomes in excess water,<sup>36</sup> whereas oleyl alcohol  
134 adopts an inverse micellar solution.<sup>26</sup>

135 The phase behavior of MO with fatty acids, such as oleic acid (OA), has previously been  
136 reported: MO:OA dispersions, stabilized by the Pluronic F127 in water, typically require an excess  
137 of 50 mol% OA to form Fd3m micellosomes,<sup>31,33</sup> and when MO:OA dispersions are made in PBS  
138 at pH 7 and 100 mM NaCl (above the  $pK_a^{app}$  of OA and hence the OA is negatively charged), over  
139 80 mol% oleic acid is required to form the Fd3m phase.<sup>37</sup>

140 Here, we have chosen to study mixtures of monoolein with oleyl alcohol, which is structurally  
141 similar to OA but is not ionisable, doped with a small amount of the pH-sensitive lipid N-(4-  
142 carboxybenzyl)-N,N-dimethyl-2,3- bis (oleoyloxy) propan-1-aminium (DOBAQ). DOBAQ is  
143 neutral at physiological pH and becomes cationic as the pH is lowered, with a  $pK_a$  of approximately  
144 6 when measured in DOPC:DOBAQ 3:1 liposomes.<sup>36</sup> Preliminary exploration of the phase  
145 behavior of MO:Olalc:DOBAQ mixtures found that 3 mol% DOBAQ was optimal to reproducibly  
146 switch between the Fd3m and  $H_{II}$  phases by lowering the pH. The phase behavior and lattice  
147 parameter ( $a$ ) dependence of MO:Olalc dispersions at a fixed 3mol% DOBAQ at 25 and 37 °C  
148 and pH 7.4 are shown in **Figure 1b**. At this fixed DOBAQ ratio the system forms hexosomes  
149 between 37 and 39 mol% Olalc. Increasing Olalc to 41 mol% at 37 °C or 42 mol% at 25 °C  
150 transforms the system to Fd3m micellosomes, with a small area of phase coexistence between 40  
151 and 41 mol% Olalc at 25 °C and 40 mol% at 37 °C.

152



153

154 **Figure 1.** Design parameters to tune the negative interfacial curvature of the nanoparticles. (a)  
 155 Increasing the amount of the weakly polar amphiphile OlAic should drive the formation of more  
 156 curved structures (top). Lowering the pH will cause DOBAQ to become cationic, increase its  
 157 effective headgroup area and electrostatic repulsion between headgroups which should result in  
 158 the adoption of less curved phases (bottom). (b) Phase behavior and the effect on the lattice  
 159 parameter of incorporating Olalc into MO dispersions, keeping the pH sensitive lipid DOBAQ  
 160 concentration fixed at 3 mol% in all samples at pH 7.4. The dashed region on the graph highlights  
 161 the composition that was further studied as a function of pH.

162

163 Olalc is non-ionisable and has a slightly smaller headgroup compared to OA and hence lower  
 164 concentrations are required to promote the Fd3m phase. This can be rationalized by increasing the  
 165 magnitude of the spontaneous inverse monolayer curvature ( $H_0$ ) towards water,<sup>38</sup> which is related  
 166 to the structural parameters of the lipids as dictated by the critical packing parameter (CPP) in  
 167 equation (1).

168 
$$CPP = \frac{v}{a_0 l} \quad (1)$$

169 where  $v$  is the molecular volume of the fluid hydrocarbon chain(s),  $l$  is the length of a fully  
170 extended hydrocarbon chain and  $a_o$  is the interfacial area per molecule at the polar-non-polar  
171 interface.

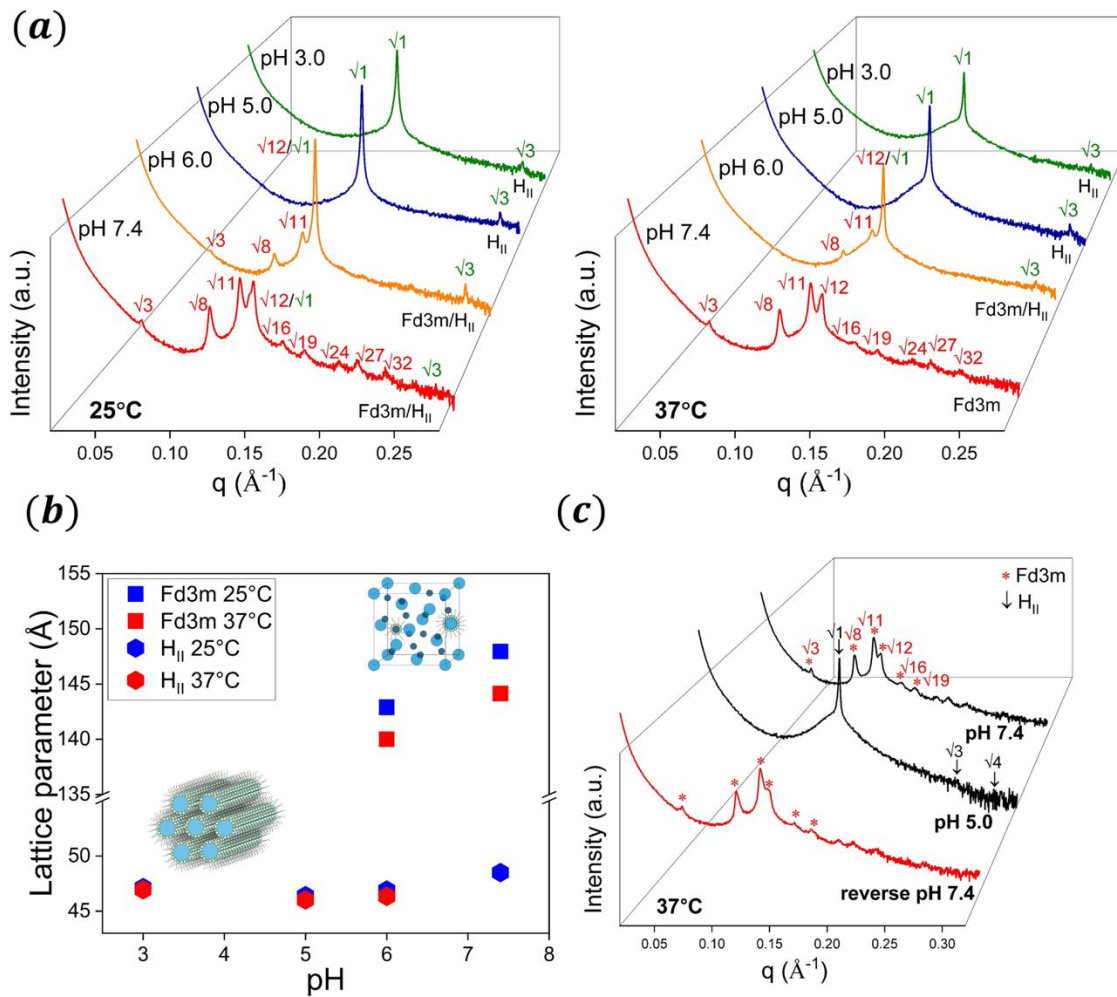
172 Increasing Olalc concentration will decrease the headgroup area driving the formation of  
173 structures with increased negative curvature. This is evident in **Figure 1b** where an increase in  
174 Olalc causes a transition from hexosomes to the more inversely curved Fd3m micellosomes.  
175 Within the pure phase regions a reduction in the lattice parameters of both phases is observed,  
176 which is explained by the reduction in water concentration with increasing mean inverse interfacial  
177 curvature.

178 These nanoparticles were engineered and envisioned for future *in vitro/vivo* applications.  
179 Consequently, a composition that formed Fd3m micellosomes at physiological temperature was  
180 chosen to further study the nanoparticle phase behavior as a function of pH. MO:Olalc:DOBAQ  
181 (56:41:3 mol%) was selected as it lies very close to the phase boundary, making it easier to trigger  
182 structural transitions between the two phases by changing the pH. The size distribution of the  
183 nanoparticles at this selected composition was determined by DLS and cryo-TEM (**Figure 3**) and  
184 is described in the cryo-TEM section later.

### 185 **Fd3m to H<sub>II</sub> transitions can be triggered by decreasing pH at fixed composition**

186 The pH dependent phase behavior as determined by SAXS shows that F127 stabilized  
187 MO:Olalc:DOBAQ (56:41:3 mol%) dispersions clearly undergo phase changes in response to pH  
188 and demonstrates that the designed system can be tuned to switch between the Fd3m and H<sub>II</sub> phases  
189 (**Figure 2a**). In these experiments, MO:Olalc:DOBAQ dispersions were originally prepared at pH  
190 7.4, aliquots taken and their pH subsequently adjusted by HCl.

191



192

193 **Figure 2.** Fd3m to H<sub>II</sub> transitions can be triggered by decreasing pH and are fully reversible. (a)  
 194 SAXS patterns of the 5 wt% F127 stabilized 56:41:3 mol % MO:Olalc:DOBAQ nanoparticles in  
 195 PBS as a function of pH at 25 °C (left) and 37 °C (right). At pH 7.4, nine Bragg peaks are observed  
 196 in the ratios of  $\sqrt{3}:\sqrt{8}:\sqrt{11}:\sqrt{12}:\sqrt{16}:\sqrt{19}:\sqrt{24}:\sqrt{27}:\sqrt{32}$  (corresponding Miller indices (hkl)  
 197 111, 220, 131, 222, 400, 331, 422, 333/511 and 440), which index as cubic space group *Fd3m* (red  
 198 label). At 25°C, the Fd3m phase coexists with a small amount of a 2D inverse hexagonal phase  
 199 (H<sub>II</sub>). At pH 6.0, the system adopts an H<sub>II</sub> phase (green label), with a Bragg peak spacing ratio of  
 200  $\sqrt{1}:\sqrt{3}$  (Miller indices (hk) are 10 and 11) indexing to plane group p6mm, coexisting with a small  
 201 amount of Fd3m phase. When the pH is  $\leq 5.0$ , only H<sub>II</sub> peaks were observed so the micellar  
 202 cubosomes have completely transformed to hexosomes. (b) Phase behavior and effect on the lattice  
 203 parameter of the nanoparticles as a function of pH. The lattice parameters of Fd3m phase decrease  
 204 with the lowering of pH from 7.4 to 6.0 at both temperatures, then the Fd3m completely transforms  
 205 to an H<sub>II</sub> phase when the pH is 5.0. (c) Reversible structural transitions triggered by pH at 37 °C:  
 206 the pH of the dispersion was decreased from 7.4 to 5.0 (black curve) using HCl and then increased  
 207 back to 7.4 (red curve) using NaOH. Indexing of the Fd3m (only the first 6 reflections are indexed  
 208 for clarity) and the H<sub>II</sub> Bragg peaks are marked with red stars and black arrows respectively. There

209 is no significant change in the lattice parameter of the Fd3m phase and no additional phases were  
210 observed before and after the pH switch, highlighting that the transition is fully reversible.

211  
212

213 At physiological pH, the system forms Fd3m micelles whereas at acidic pH the  
214 nanoparticles transform to hexosomes. This is attributed to the pH-sensitive behavior of DOBAQ,  
215 which is neutral at pH 7.4 due to a quaternary amine present in its headgroup and becomes cationic  
216 at acidic pH via protonation of its carboxylate group. The protonation of DOBAQ imposes a  
217 change in CCP, due to an increase in the surface charge density and enhanced electrostatic  
218 repulsion between charged headgroups. This in turn, increases the effective headgroup area and  
219 hence decrease the magnitude of the monolayer spontaneous inverse curvature driving the  
220 formation of less negatively curved phases.<sup>2, 6, 39</sup>

221 **Figure 2b** shows the variation in the structure and lattice parameter of the system with pH and  
222 temperature. At 25 °C and pH 7.4, the system adopts an Fd3m phase with a lattice parameter of  
223 148 Å. An additional weak reflection occurring around  $q \approx 0.15 \text{ \AA}^{-1}$  is due to a coexisting H<sub>II</sub> phase  
224 with a lattice parameter of 48 Å. At 37 °C and pH 7.4 the system adopts a pure Fd3m phase with  
225 a lattice parameter of 145 Å. Upon decreasing the pH from 7.4 to 6.0, the system transforms to  
226 hexosomes. This is supported by recording the characteristic  $\sqrt{3}$ -reflection of the H<sub>II</sub> phase (**Figure**  
227 **2a**) with a small contribution of coexisting Fd3m micelles at both 25 and 37 °C. We note that  
228 diffraction peak intensities scale with the underlying material's volume fraction. Peak intensities  
229 can therefore be used to estimate the amount of material adopted by each respective phase. This  
230 transition is in agreement with the pK<sub>a</sub> of DOBAQ measured by Walsh *et al.* in a liposomal  
231 formulation (pH  $\approx$  6.0).<sup>36</sup> Although the apparent pK<sub>a</sub> of a lipid has been shown to give rise to a  
232 distribution of pK<sub>a</sub> values that is dependent on the curvature and the phase adopted,<sup>31</sup> our results  
233 in Figure 2a are in line with the pK<sub>a</sub> estimate for DOBAQ reported by Walsh *et al.*<sup>36</sup> We further

234 note, that the Bragg peaks of the Fd3m phase shift to higher  $q$  from pH 7.4 to 6, corresponding to  
235 a decrease in  $a_{Fd3m}$  to 140 Å and 142 Å at 25 °C and 37 °C respectively. The effect of increasing  
236 temperature, which will increase the chain splay and  $H_0$  resulting in a decrease in the lattice  
237 parameter of a mesophase, is consistent with the behavior seen here and with most lyotropic liquid  
238 crystalline formulations. On the contrary, the observation of a decrease in lattice parameter with  
239 an increase in charge is at first instance counter-intuitive, because an increase in charge should  
240 reduce  $H_0$  and hence cause the lattice parameter of the Fd3m phase to increase. This trend could  
241 be rationalized by considering the size of the nanoparticles which is also highlighted in the  
242 subsequent section on cryo-TEM data. As seen in **Figures 3** and **4**, Fd3m micellosomes have a  
243 range of sizes and vary in their lattice parameters, with smaller nanoparticles generally displaying  
244 bigger lattice parameters and larger nanoparticles displaying smaller lattice parameters. The larger  
245 nanoparticles offer a bigger confinement volume for lyotropic liquid crystals to form, and as a  
246 consequence are less prone to structural defects and repulsive membrane undulation forces which  
247 will result in smaller lattice spacings and also render them more stable. We hypothesize that at pH  
248 6, close to the pKa of DOBAQ, the weak reflections from the Fd3m structure are due to a few  
249 remaining more stable, relatively bigger Fd3m nanoparticles which have smaller lattice parameters  
250 (**Figure 2b**). Within the timescale of the experiments presented here, by the time the nanoparticles  
251 were mixed with acid or base, loaded in a sample holder and a SAXS pattern collected (15 minutes  
252 or less), the nanoparticles had already switched their structure, giving an upper limit to the response  
253 time for structural switching in these nanoparticles.

254

255 At pH 5.0, only the H<sub>II</sub> phase was observed and hence the system has completely transformed  
256 from the initial Fd3m phase. Further decreasing the pH to 3 did not alter the phase behavior and  
257 the lattice parameter of the H<sub>II</sub> phase varied little (maximum  $\pm 2$  Å) across all pH values measured.

258

### 259 **pH-triggered Fd3m to H<sub>II</sub> transitions are reversible**

260 To evaluate the potential to reverse the structural transition in the designed system at 37 °C, the  
261 pH of the sample was first lowered from pH 7.4 where the system adopted a pure Fd3m phase, to  
262 pH 5.0, where only the H<sub>II</sub> phase was observed. The pH was then subsequently raised back to 7.4  
263 in the same sample leading to the reformation of the Fd3m phase. SAXS data demonstrate the  
264 reversibility of the Fd3m to H<sub>II</sub> transition by adjusting the pH of the PBS dispersions with NaOH  
265 or HCl (**Figure 2c**). The lattice parameter of the sample in the Fd3m phase before (144.9 Å) and  
266 after reversing the pH back to pH 7.4 (147.1 Å) is very similar, highlighting the truly reversible  
267 responsiveness of the system. The structure reversibility of the system is due to the protonation  
268 and deprotonation of the DOBAQ headgroup. When the pH is 7.4, the DOBAQ headgroup  
269 deprotonates and becomes neutral whereas at lower pH protonation causes the headgroup to  
270 become cationic. Repulsions between the gradually protonating or deprotonating carboxylic group  
271 of 3 mol% DOBAQ embedded at the lipid-water interface, modifies the system's spontaneous  
272 curvature.

273 MO can hydrolyze over long periods of time, producing oleic acid and glycerol<sup>40</sup> and the apparent  
274 pK<sub>a</sub> of oleic acid in MO:OA dispersions has been measured to be between 6-7.<sup>31</sup> Even if a small  
275 amount of MO has hydrolyzed, it has an insignificant effect on the phase transition as a.) samples  
276 consistently and reversibly switch between the Fd3m and H<sub>II</sub> phases at different pH values,  
277 indicating a true equilibrium phase behavior and b.) if instead a moderate amount of OA was

278 present, then this would cause the system to transform to an H<sub>II</sub> phase at pH 7.4 due to OA having  
279 a negative charge, leading to a decrease in curvature, and it would also hamper the formation of  
280 an H<sub>II</sub> phase at low pH due to being neutral, promoting more curved interfaces, such as in the  
281 Fd3m. This phase behavior is the exact opposite to what we observe here, so we conclude that  
282 Fd3m to H<sub>II</sub> transition at low pH is clearly dominated by the protonation/ deprotonation of the  
283 DOBAQ headgroup.

284 Note that both the H<sub>II</sub> and Fd3m phases have significant chain packing frustration, which might  
285 be thought to potentially lead to an out of equilibrium trapping of one or other of these phases. For  
286 example, during temperature jumps on MO dispersions, Dong *et al.*<sup>41</sup> showed supercooling effects  
287 as well as non-equilibrium structures appearing for more than thirteen hours before they returned  
288 to the equilibrium structure. As mentioned above, such effects are not seen here and we estimate  
289 our pH induced transitions to occur on the minute timescale based on our experimental  
290 observations and our previous studies of hydrostatic pressure induced Fd3m-H<sub>II</sub> phase transitions  
291 in similar lipid systems.<sup>42</sup>

292 The nanostructure of the designed system can be easily tuned by only a very small amount of  
293 pH-sensitive lipid, and shows the excellent pH sensitivity and selectivity of this system compared  
294 to previous studies where large amounts of ionisable lipids were required to switch between these  
295 two structures and/or significant changes in ionic strength of the buffer. Moreover, whilst an Fd3m  
296 to H<sub>II</sub> transition has been reported in the literature by increasing pH (although none have  
297 demonstrated this at 37 °C), this is the first example of an Fd3m to H<sub>II</sub> transition from physiological  
298 to acidic pH. This transition could potentially be advantageous in nanomedicine, where a  
299 hydrophilic active could be encapsulated into the inverse micelles of the Fd3m phase significantly  
300 hindering its release in the serum, but by rearranging to a porous H<sub>II</sub> phase, e.g. in the endosome,

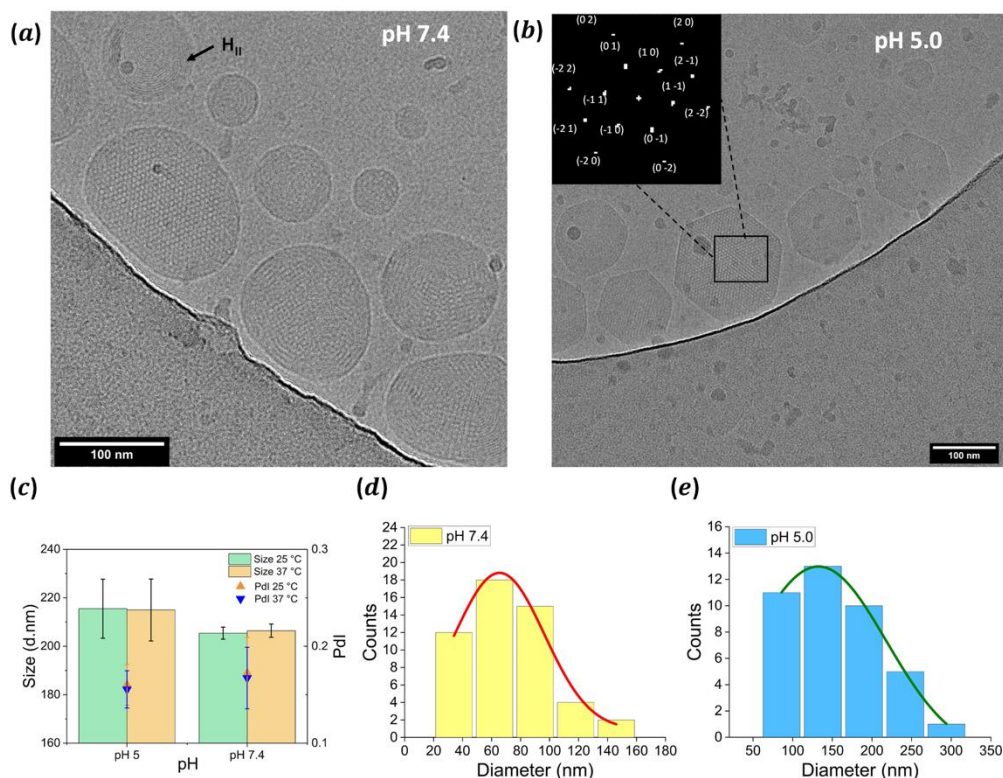
301 can facilitate release. As an example, the diffusion coefficient of glucose from a system adopting  
302 the H<sub>II</sub> phase was shown to be approximately 15 times that observed in the Fd3m phase in bulk  
303 mesophases however how this translates to LCNPs is not known.<sup>27</sup>

304 By varying the position of the Gibbs-dividing surface to be between 13-15Å (see **Supporting**  
305 **Information** Section 1) we estimate the diameters of the small and big micelles to be between  
306 22.7-26.7 and 34.5-38.5 Å respectively. Consequently, any hydrophilic molecule or globular  
307 protein with a diameter of up to 26.7 Å can be fully encapsulated into the Fd3m micellesomes and  
308 any molecule with a diameter of up to 38.5 Å can be partially incorporated into the big micelles of  
309 the Fd3m structure.

310 **Cryogenic Transmission Electron Microscopy (Cryo-TEM) facilitates quantitative**  
311 **structural characterization of individual LCNPs**  
312

313 The cryo-TEM images of the designed MO:Olalc:DOBAQ 56:41:3 mol% system confirmed the  
314 pH-triggered nanostructural transitions observed by SAXS. At pH 7.4, the cryo-TEM image  
315 indicates the presence of Fd3m micellesomes coexisting with as small amount hexosomes, with  
316 the Fd3m micellesomes dominating in the dispersions (**Figure 3a**) at 25 °C. By contrast, only  
317 hexosomes were observed at pH 5.0 (**Figure 3b**).

318



319

320 **Figure 3.** Representative cryo-TEM images of the MO:Olalc:DOBAQ 56:41:3 mol% system  
 321 prepared at 25 °C and their size distributions. (a) Fd3m micelles at pH 7.4 coexisting with a  
 322 small amount of hexosomes (black arrow), which likely give rise to the weak intensity of the  $\sqrt{1}$   
 323 peak in the SAXS data in Figure 2a. Both SAXS and cryo-TEM data are in agreement that the  
 324 dominating phase at pH 7.4 at 25 °C is Fd3m. (b) pure hexosomes at pH 5.0. The insert in panel  
 325 b shows the corresponding intensity of the fast Fourier transform (FFT) applied to the black box  
 326 region of the individual nanoparticle and the assigned Miller indices. (c) Dynamic light scattering  
 327 (DLS) data of MO:Olalc:DOBAQ 56:41:3 mol% nanoparticles in PBS at different pH at 25 °C  
 328 (green) and 37 °C (orange). At 25 °C, Fd3m micelles at pH 7.4 have a mean size of ~205  
 329 nm, whilst hexosomes are ~216 nm at pH 5; At 37 °C Fd3m micelles have a mean size of  
 330 ~206 nm and hexosomes ~215 nm. (d) and (e) Cryo-TEM size distribution of nanoparticles  
 331 hydrated at pH 7.4 and pH 5.0 respectively. Histograms were calculated from 51 nanoparticles at  
 332 pH 7.4 and 40 for pH 5.0 and fitted to a Gaussian function. From the fit we obtain a mean of 65  
 333 and 132 nm for the nanoparticles at pH 7.4 and pH 5 respectively. Both DLS and Cryo-TEM data  
 334 show nanoparticles at pH 5.0 generally have a slightly larger size compared to that at pH 7.4.

335  
 336

337 The particle size distribution of the nanoparticles at 25 and 37 °C was investigated using dynamic  
 338 light scattering (DLS) and the results are shown in **Figure 3c**. The Fd3m micelles at pH 7.4  
 339 have a mean size of ~205 and 206 nm, whereas the hexosomes at pH 5 have a mean size of ~216

340 and 215 nm, at 25 and 37 °C respectively. The error bars are the mean plus the standard deviation  
341 of the average value of four different samples, each measured five times. The DLS results at 25  
342 °C were compared with the nanoparticle size analysis from Cryo-TEM data (51 nanoparticles  
343 analyzed at pH 7.4 and 40 at pH 5.0) shown in **Figure 3d** and **3e**. The histograms were fitted to a  
344 Gaussian function and we obtain a mean size of 65 and 132 nm for the nanoparticles at pH 7.4 and  
345 pH 5, respectively. The mean size of the nanoparticles calculated differs between the two  
346 techniques, as DLS weighs the size distribution differently with larger particles emphasized as  
347 they scatter light more strongly whereas cryo-TEM often excludes larger particles from the thin  
348 ice films, emphasizing smaller particles in these polydisperse populations. Nonetheless, there is a  
349 clear trend that hexosomes are larger than the micellar cubosomes. This is because a decrease in  
350 pH leads to protonation of the DOBAQ headgroup resulting in a repulsive force at the lipid-water  
351 interface which pushes the elongation of the Fd3m micellar ‘pockets’ to form a tubular structure  
352 in the H<sub>II</sub> phase and an overall increase in the water concentration. However, the overall increase  
353 in water volume is only about 6% when hexosomes are formed, which would only account for a  
354 2% increase in particle size (for estimations please see **Supporting information** Section 1), thus  
355 this cannot be the only explanation for the more strongly differing particle sizes. On a mesoscopic  
356 level though, there is an unneglectable difference. While the micellosomes are spherical in shape  
357 and hence display a maximized volume to surface ratio, hexosomes are by no means perfectly  
358 spherical. They display different shapes, like flat hexagonal prisms (**Figure 3b**), and often possess  
359 even “spinning top-like” structures.<sup>43</sup> In any case, their shape deviates significantly from that of a  
360 sphere, and hence, the apparent mean hydrodynamic size of hexosomes is bigger, whilst their  
361 volume has not increased by much. This apparent size increase of hexosomes is even more

362 pronounced in our cryo-TEM measurements, since we measured the diameter of the hexagonal  
363 prism section, whilst not considering the perpendicular short extension of the hexosomes.

364  
365 Traditionally, cryo-TEM cannot be used to unambiguously determine the space group of  
366 lyotropic liquid crystalline phases due to the low resolution of the images leading to only a couple  
367 of peaks to be observed after applying a fast Fourier transform to the image.<sup>44</sup> However, it is a  
368 powerful complementary technique to SAXS. Whilst cubosomes based on bicontinuous cubic  
369 phases, and hexosomes are easier to visualize with cryo-TEM and give rise to a number of peaks  
370 in their FFTs,<sup>45-46</sup> cryo-TEM images of Fd3m micelles reported to date in the literature are  
371 of very low resolution, which is insufficient for the visualization of the internal nanostructure of  
372 the phase.

373 Here we have been able to obtain high resolution images and directly visualize the internal  
374 structure of the Fd3m nanoparticles along two viewing orientations, which allow us to resolve the  
375 large and small micelles of the Fd3m structure and calculate structural information using cryo-  
376 TEM for the first time.

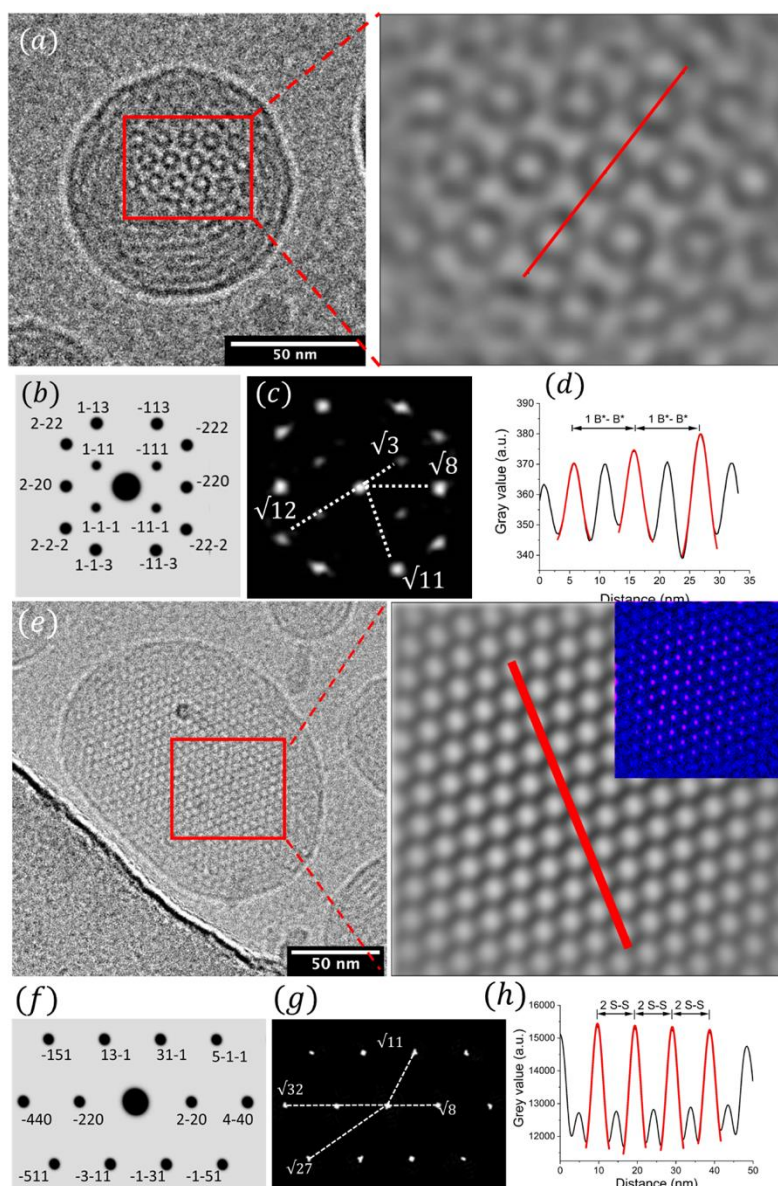
377

378 **Figure 4** shows detailed images of Fd3m nanoparticles in two different orientations, image  
379 analysis, indexing and simulated TEM diffraction patterns. **Figure 4a** highlights an Fd3m  
380 micelle along the [110] viewing direction with respect to the electron beam. The simulated  
381 TEM diffraction pattern from an Fd3m phase diffraction pattern viewed down the (110) plane  
382 normal (**Figure 4b**) is in excellent agreement with the experimentally determined FFT pattern.  
383 **Figure 4c** shows the FFT from the image in **Figure 4a** in which the  $\sqrt{3}$ ,  $\sqrt{8}$ ,  $\sqrt{11}$  and  $\sqrt{12}$   
384 reflections, corresponding to Miller planes (111), (220), (311) and (222) can be clearly observed.  
385 Each theoretical reflection from the simulated diffraction pattern indexed in **Figure 4b**

386 corresponds to the same reflection in **Figure 4c**. The lattice parameter of the nanoparticle in **Figure**  
387 **4a** was determined to be 149.3 Å (see also **Supporting Information** Section 2 for additional  
388 information on determining the lattice parameter).

389 **Figure 4e** shows an Fd3m nanoparticle aligned along the [114] direction with respect to the  
390 electron beam in which the  $\sqrt{8}$ ,  $\sqrt{11}$ ,  $\sqrt{27}$  and  $\sqrt{32}$  reflections, corresponding to Miller planes (220),  
391 (311), (511) and (440) were observed. Each theoretical reflection from an Fd3m phase viewed  
392 down the (114) plane normal and indexed in **Figure 4f** directly matches the experimentally  
393 determined reflections in **Figure 4g**. The lattice parameter of the particle in **Figure 4e** was  
394 determined to be 137.0 Å based on the FFT analysis.

395 The lattice parameters of the individual nanoparticles calculated from the cryo-TEM data are  
396 slightly different to those obtained by SAXS, which is expected, as SAXS gives the average lattice  
397 parameter of all the nanoparticles in the measured sample whilst we focus on specific nanoparticles  
398 for the cryo-TEM analysis. Based on the cryo-TEM images collected, we observe that generally  
399 nanoparticles which have a smaller lattice parameter tend to be larger in size. This finding supports  
400 our hypothesis that smaller Fd3m nanoparticles undergo a faster structural transition compared to  
401 larger particles, as they are expected to contain relatively more defects (cp. discussion above) and  
402 are thus less stable.



403

404 **Figure 4.** High resolution cryo-TEM images allow direct visualization of the internal structure of  
 405 the Fd3m nanoparticles. (a) Cryo-TEM image on an Fd3m micelle of MO:Olalc:DOBAQ  
 406 56:41:3 mol% prepared at 25 °C and pH 7.4. The nanoparticle is aligned along the [110] orientation  
 407 with respect to the electron beam. The red box indicates the region used to apply the FFT shown  
 408 in 4c and the zoomed-in region on the right hand side shows the inverse FFT of 4c (after application  
 409 of rolling background subtraction and Gaussian blur), and was used to determine the  $d_{B^*-B^*}$   
 410 distance indicated by the red line. (b) Simulated transmission electron microscopy (TEM)  
 411 diffraction pattern viewed down the (110) plane normal of an Fd3m phase with assigned Miller  
 412 indices and (c) the corresponding intensity of the FFT applied to the red box region of 4a which is  
 413 in excellent agreement with the simulated pattern. Each theoretical reflection from the simulated  
 414 pattern indexed in 4b corresponds to the same reflection in 4c. (d) Gaussian fitting of the intensity  
 415 profile along the red line of the inverse FFT, shown in the zoomed in region of 4a, gave an average

416 distance between two interval big micelles ( $d_{B^*-B^*}$ ) of 105.5 Å. The lattice parameter of the  
 417 nanoparticle in 4a was determined to be 149.3 Å, which gives a theoretical  $d_{B^*-B^*}$  value of 105.5  
 418 Å. (e) cryo-TEM image of an Fd3m nanoparticle aligned along the [114] orientation with respect  
 419 to the electron beam. The red box indicates the region used to apply the FFT shown in 4g and the  
 420 zoomed-in region on the right hand side shows the inverse FFT of 4g (after application of rolling  
 421 background subtraction and Gaussian blur), and was used to determine the  $d_{S-S}$  distance indicated  
 422 by the red line. The inset shows the overlay of the raw image of 4e on the left shown in blue and  
 423 the inverse FFT on the right shown in magenta which are in excellent agreement. (f) Simulated  
 424 transmission electron microscopy (TEM) diffraction pattern viewed down the (114) plane normal  
 425 of an Fd3m phase with assigned Miller indices and (g) the corresponding intensity of the FFT  
 426 applied to the red box region of 4e which is in excellent agreement with the simulated pattern.  
 427 Each theoretical reflection from the simulated pattern indexed in 4f corresponds to the same  
 428 reflection in 4g. (h) Gaussian fitting of the intensity profile along the red line of the inverse FFT,  
 429 shown in the zoomed in region of 4e, gave an average plane to plane distance of the small micelles  
 430 ( $d_{S-S}$ ) of 48.5 Å. The lattice parameter of the nanoparticle in 8a was determined to be 137 Å,  
 431 which gives a theoretical  $d_{S-S}$  value of 48.4 Å.  
 432

433 The high resolution cryo-TEM images have allowed us to direct visualize the large and small  
 434 micelles of the Fd3m structure (eight large and sixteen small micelles per unit cell), determine the  
 435 micelle positions and compare them to theoretical distances for the Fd3m structure.

436 From geometry,<sup>47</sup> the big (B) micelle-to-micelle distance is given by equation 2:

$$437 \quad d_{B-B} = \frac{\sqrt{3}}{4} a \quad (2)$$

438 and the small (S) micelle-to-micelle distance is given by:

$$439 \quad d_{S-S} = \frac{\sqrt{2}}{4} a \quad (3)$$

440  
 441 **Figure 4a** shows an Fd3m micellosome aligned along the [110] orientation. The distribution of  
 442 the different micelles along the (110) section will depend on where the section cuts through the  
 443 plane along the z direction. Here only the big micelles are seen, however this does not represent  
 444 the  $d_{B-B}$  micelle-to-micelle distance defined above which is the smallest distance between two  
 445 adjacent big micelles, but instead what we define as the  $d_{B^*-B^*}$  distance, which is the distance

446 between two interval big micelles (i.e. two *next nearest* big micelles, see B\*-B\* distance in figure  
447 **S3b**) and is given by equation 4 (see also **Supporting Information** Section 3):

$$448 \quad d_{B^*-B^*} = 2d_{S-S} = \sqrt{\left(\frac{8}{3}\right)}d_{B-B} = \frac{\sqrt{2}}{2}a_{Fd3m} \quad (4)$$

449  
450 Further discussion on determining the  $d_{B^*-B^*}$  distance as well as comparing the excellent  
451 agreement of the inverse FFT (**Figure S3a**) obtained from **Figure 4c** with some 2-D serial sections  
452 of the 3-D electron density map from a previously published DOPC:DOG 1:2 mol% system  
453 adopting an Fd3m phase (**Figures S3b** and **S3c**)<sup>42</sup> can be found in **Supporting Information**  
454 Section 3.

455 Experimentally, the B\*-B\* distance was determined by taking the inverse FFT of **Figure 4c**, which  
456 has been background subtracted. The resulting, Gaussian blurred, inverse FFT shown on the right  
457 of **Figure 4a** was used to determine the B\*-B\* ( $d_{B^*-B^*}$ ) distance by Gaussian fitting (**Figure 4d**)  
458 of its intensity profile along the red line in **Figure 4a** (right). The average  $d_{B^*-B^*}$  distance  
459 measured was 105.5 Å which is identical to the theoretical distance of 105.5 Å based on the  
460 experimentally determined lattice parameter of 149.3 Å (equation 4).

461 **Figure 4e** shows an Fd3m micellosome aligned along the [114] orientation and highlights the  
462 small micelles of the Fd3m phase. Based on the reflections of the FFT in **Figure 4g**, the lattice  
463 parameter was determined to be 137 Å, which gives a theoretical  $d_{S-S}$  micelle-to-micelle distance  
464 of 48.4 Å (equation 2). Note the  $\sqrt{8}$  reflection also corresponds to the S-S micelle distance. The  
465  $d_{S-S}$  distance was determined by taking the inverse FFT of **Figure 4g**, which has been background  
466 subtracted. The resulting, Gaussian blurred, inverse FFT is shown in **Figure 4e** (right) was used  
467 to determine the  $d_{S-S}$  distance by Gaussian fitting (**Figure 4h**) of its intensity profile along the red  
468 line in **Figure 4e** (right). The overlay of the raw image of **Figure 4e** (left) shown in blue and

469 inverse FFT (from **Figure 4g**) shown in magenta are in excellent agreement (**Figure 4a**, right,  
470 inset). It should be noted that in the [114] direction,  $d_{S-S}$  does not correspond to the distance  
471 between two adjacent small micelles as shown in **Figure S3b** for the (110) section but is instead  
472 the plane to plane distance of the small micelles in this projection (**Figure 4e** (right), see also  
473 **Figure S4**). The experimentally determined S-S plane distance (**Figure 4h**) and the (220)  
474 reflection from **Figure 4g** were 48.5 and 48.3 Å respectively and match the theoretical distance of  
475 48.4 Å determined above.

476

## 477 CONCLUSION

478 We have been able to generate highly sensitive pH responsive lyotropic liquid crystalline  
479 nanoparticles that require only a very small amount (3 mol%) of pH sensitive lipid to switch  
480 between a compartmentalized internal structure based on space group Fd3m at physiological pH  
481 to an accessible porous 2D hexagonal structure when the pH is  $\leq 6$  at both 25 and 37 °C. The  
482 transition is fully reversible by tuning the inverse spontaneous curvature by the protonation or  
483 deprotonation of the pH sensitive lipid's headgroup. The internal symmetry of the nanoparticles  
484 was confirmed by SAXS and cryo-TEM. Imaging of Fd3m nanoparticles has been challenging  
485 with cryo-TEM however we have managed to acquire high resolution images of them and directly  
486 visualize the structure in unprecedented detail for the first time. Depending on the direction the  
487 particles are aligned with respect to the electron beam we can resolve the large and small inverse  
488 micelles of the Fd3m phase which allowed us to calculate structural information such as the  
489 positions and distances of the two different sized micelles and compare these to theory based on  
490 geometrical considerations. These promising findings could pave the way to developing superior  
491 stimuli-responsive soft nanoparticle formulations that change their connectivity upon encountering

492 acidic pH, which is known for example to be highly important both in human disease as well as  
493 plant physiology and crop performance. They can potentially benefit a range of downstream  
494 applications in the biomedical, food, agrochemical and environmental remediation industries.

495

## 496 **EXPERIMENTAL SECTION**

497

498 **Preparation of MO/Olalc/DOBAQ nanoparticles.** Monoolein (MO; was a kind gift from  
499 Croda Personal Care, Goole, UK), Oleyl alcohol (Olalc; Sigma Aldrich, Gillingham, UK), N-(4-  
500 carboxybenzyl)-N,N-dimethyl-2,3-bis(oleoyloxy)propan-1-aminium (DOBAQ; Avanti polar  
501 lipids, AL, USA) were weighted and dissolved in chloroform (Sigma-Aldrich, Gillingham, UK),  
502 then mixed at the desired MO:Olalc:DOBAQ molar ratios. MO had a purity of >92% (containing  
503 a minimum of 92% monoester and maximum 8% diester) whilst the rest of the lipids had a purity  
504 of >99% and were used without further purification. The chloroform solutions were dried using a  
505 stream of N<sub>2</sub> gas and the dry thin films were left under vacuum overnight to remove any residual  
506 organic solvent. Thin films were then heated to 60 °C and hydrated with phosphate-buffered saline  
507 buffer (PBS; Sigma-Aldrich, Gillingham, UK) containing 6.923 mg/ml Pluronic F127, 5 wt%  
508 F127 of total lipids, (Sigma-Aldrich, Gillingham, U.K.) to achieve a sample concentration of 100  
509 mg/ml. Dispersed samples were prepared by tip sonication (VibraCell 750 with a stepped microtip,  
510 Sonics & Materials Inc, Newtown, USA) for 30 minutes in pulse mode (1s pulse, 1s break) at 35%  
511 of its maximum power (750 W). The pH of the NP dispersions was readjusted to 7.4 using 0.1M  
512 NaOH (Fisher Scientific, Loughborough, UK) or 0.1M HCl (Fisher Scientific, Loughborough,  
513 U.K.). Samples for SAXS measurements were measured after the pH was switched under two  
514 conditions: 1) immediately after switching and 2) after equilibration at 37 °C overnight. SAXS  
515 patterns of samples under condition 1 were collected at 37 °C whereas samples SAXS patterns for

516 samples under condition 2 were collected at both 25 and 37 °C. The pH of the dispersed  
517 nanoparticles was first gradually decreased from 7.4 to 3.0, then increased back to 7.4 while taking  
518 out samples at each selected pH point for SAXS measurements at both 25 °C and 37 °C. For the  
519 dynamic light scattering and cryogenic transmission electron microscopy data, lipid nanoparticles  
520 were hydrated by PBS at pH 7.4 or pH 5.0 directly and allowed to equilibrate overnight at 37 °C  
521 before measurement.

522

523 **Synchrotron Small-Angle X-ray Scattering (SAXS).** Synchrotron SAXS data were collected  
524 on beamline I22 at Diamond Light Source. The synchrotron X-ray beam was set to 18 keV which  
525 corresponds to a wavelength of 0.69 Å. The sample to detector distance was set at 6 or 8.7 m and  
526 the 2-D powder diffraction patterns were recorded on a Pilatus 2M detector. SAXS data were  
527 analyzed using the DAWN software.<sup>48-49</sup> The lattice parameters of the Fd3m and H<sub>II</sub> phases were  
528 calculated using the equations below:

529

$$530 \quad a_{Fd3m} = \frac{2\pi}{q_{hkl}} \sqrt{h^2 + k^2 + l^2} \quad (5)$$

$$531 \quad a_{H_{II}} = \frac{4\pi}{\sqrt{3} q_{hk}} \sqrt{h^2 + k^2 + hk} \quad (6)$$

532

533 where  $q_{hkl}$  or  $q_{hk}$  is the scattering vector and  $hkl$  or  $hk$  are the Miller indices of a given Bragg  
534 peak. Samples were equilibrated at 25 °C and 37 °C for 5 min before taking measurements.

535

536 **Dynamic Light Scattering (DLS).** For DLS measurements, particles were made at a  
537 concentration of 5 mg/mL. In total, four different samples were measured and each sample was  
538 measured five times. Samples were diluted to 25 µg/mL by isotonic PBS at different pH before

539 DLS measurement. The mean hydrodynamic radius and polydispersity index width (PDI) of the  
540 nanoparticles were measured at pH 7.4 and pH 5.0 using a Malvern Zetasizer Nano ZSP instrument  
541 (Malvern Panalytical, Malvern, UK) equipped with a 633 nm helium-neon laser. Samples were  
542 measured at 25 °C or 37 °C at a fixed 173° backscattering angle. The refractive index and  
543 absorption of the nanoparticles was set as 1.46 and 0.001 respectively using values for pure MO.  
544 The refractive index of PBS is 1.334 and its viscosity was set to 0.9110 mPa.s at 25 °C and 0.7130  
545 mPa.s at 37 °C.

546

547 **Cryogenic-transmission electron microscopy (Cryo-TEM).** Samples were diluted once (final  
548 concentration of 50 mg/ml) in isotonic PBS at the required pH for the morphological  
549 characterization using cryo-TEM. In brief, 3 µL of the diluted sample was applied to freshly glow  
550 discharged Cu QUANTIFOIL grids (R2/R2, 300 or 400 mesh) with a hold time of 30 s. The  
551 carbon-coated grids were glow discharged at 10 mA for 20 s for samples at pH 7.4 and 30 s for  
552 samples at pH 5.0. The grids were blotted for 6 s with a blotting force of 7 at 25 °C under 100%  
553 relative humidity, then plunged into liquid ethane using a Vitrobot™ mark IV (Thermo/FEI).  
554 Grids were kept under liquid nitrogen before measurement.

555 Data acquisition was carried out on a Titan KRIOS microscope (Thermo Fisher Scientific, US)  
556 with an accelerating voltage of 300 kV and a defocus value of -1 µm at a nominal magnification  
557 of 45k or 75k. The pixel size for these images were 1.76 and 1.065 Å, respectively. Image  
558 processing was done using Fiji.<sup>50</sup> The Fast Fourier Transforms (FFTs) of the raw images were  
559 background subtracted. The d-spacing of each reflection in the FFT was determined using  
560 TrackMate.<sup>51</sup> The micelle distances were calculated from the inverse FFTs after application of  
561 rolling background subtraction and Gaussian blur using Fiji.

562

563 **Simulation of TEM diffraction patterns.** The program CrystalMaker® (CrystalMaker  
564 Software Ltd, Oxford, England-[www.crystallmaker.com](http://www.crystallmaker.com)) was used to visualize 2-D sections (110  
565 and 114 planes) through the model structure of the Fd3m cubic phase. Fd3m origin 2 (at  $\bar{3}m$ ) was  
566 used. These sections were then sent to the SingleCrystal™ program to simulate transmission  
567 electron microscopy (TEM) diffraction patterns.

568

569 ASSOCIATED CONTENT

570 **Supporting Information**

571 Discussion on the estimation of micellosome and hexosome size ratios, details on the calculation  
572 of lattice parameters from cryo-TEM data and determination of the micelle positions in Fd3m  
573 nanoparticles. This material is available free of charge via the Internet at <http://pubs.acs.org>.

574

575 **AUTHOR INFORMATION**

576 **Corresponding Author**

577 **Arwen I.I. Tyler** - School of Food Science and Nutrition, University of Leeds, Leeds, LS2 9JT,  
578 United Kingdom

579 Email: [A.I.I.Tyler@leeds.ac.uk](mailto:A.I.I.Tyler@leeds.ac.uk)

580

581 **Authors**

582 **Zexi Xu** - School of Food Science and Nutrition and School of Chemistry, University of  
583 Leeds, Leeds, LS2 9JT, United Kingdom

584 **John M. Seddon** - Department of Chemistry, Imperial College London, London, W12  
585 0BZ, United Kingdom.

586 **Michael Rappolt** - School of Food Science and Nutrition, University of Leeds, Leeds, LS2  
587 9JT, United Kingdom.

588 **Paul A. Beales** - School of Chemistry and Astbury Centre for Structural Molecular  
589 Biology, University of Leeds, Leeds, LS2 9JT, United Kingdom

590

### 591 **Author Contributions**

592 A.I.I.T. conceived and designed the experiments. J.M.S, P.A.B., M.R. and A.I.I.T contributed to  
593 study design. Z.X. performed all the experiments. Z.X., M.R. and A.I.I.T. analyzed the data. Z.X.,  
594 P.A.B., M.R. and A.I.I.T. interpreted the results. Z.X. M.R. and A.I.I.T co-wrote the manuscript.  
595 All authors discussed the results and commented on the manuscript.

### 596 **Funding Sources**

597 The research was supported by start-up funding awarded to A.I.I.T. from the University of Leeds  
598 as a well as a PhD scholarship awarded to Z.X.

599

### 600 **Notes**

601 The authors declare no competing financial interest.

602

### 603 **ACKNOWLEDGMENTS**

604 We thank Diamond Light Source for the award of synchrotron beamtimes (SM18027-1, SM22659-  
605 1 and SM24530-1) as well as Dr. Andy Smith, Dr. Tim Snow and Professor Nick Terrill for their  
606 support and assistance. We thank Dr. Aleks Ponjavic from the University of Leeds for help with

607 some aspects of image processing and analysis and drawing figures. We also thank Dr. Rebecca  
608 Thompson from the Astbury Biostructure Facility and Rashmi Seneviratne from the School of  
609 Chemistry at the University of Leeds for their support with Cryo-TEM. The FEI Titan Krios  
610 microscope used was funded by the University of Leeds (UoL ABSL award) and Wellcome Trust  
611 (108466/Z/15/Z). The Bragg Centre for Materials Research at the University of Leeds is also  
612 acknowledged.

613

## 614 **References**

- 615 1. Nguyen, T. H.; Hanley, T.; Porter, C. J.; Boyd, B. J., Nanostructured liquid crystalline  
616 particles provide long duration sustained-release effect for a poorly water soluble drug after oral  
617 administration. *J Control Release* **2011**, *153* (2), 180-186.
- 618 2. Kim, H.; Leal, C., Cuboplexes: Topologically Active siRNA Delivery. *ACS Nano* **2015**, *9*  
619 (10), 10214-10226.
- 620 3. Praca, F. S. G.; Medina, W. S. G.; Petrilli, R.; Bentley, M. V. L. B., Liquid Crystal  
621 Nanodispersions Enable the Cutaneous Delivery of Photosensitizer for Topical PDT: Fluorescence  
622 Microscopy Study of Skin Penetration. *Current Nanoscience* **2012**, *8* (4), 535-540.
- 623 4. Jain, V.; Swarnakar, N. K.; Mishra, P. R.; Verma, A.; Kaul, A.; Mishra, A. K.; Jain, N. K.,  
624 Paclitaxel loaded PEGylated glyceryl monooleate based nanoparticulate carriers in chemotherapy.  
625 *Biomaterials* **2012**, *33* (29), 7206-7220.
- 626 5. Rizwan, S. B.; McBurney, W. T.; Young, K.; Hanley, T.; Boyd, B. J.; Rades, T.; Hook, S.,  
627 Cubosomes containing the adjuvants imiquimod and monophosphoryl lipid A stimulate robust  
628 cellular and humoral immune responses. *J Control Release* **2013**, *165* (1), 16-21.
- 629 6. Zhai, J.; Fong, C.; Tran, N.; Drummond, C. J., Non-Lamellar Lyotropic Liquid Crystalline  
630 Lipid Nanoparticles for the Next Generation of Nanomedicine. *ACS Nano* **2019**, *13* (6), 6178-  
631 6206.
- 632 7. Ganta, S.; Devalapally, H.; Shahiwala, A.; Amiji, M., A review of stimuli-responsive  
633 nanocarriers for drug and gene delivery. *J Control Release* **2008**, *126* (3), 187-204.
- 634 8. Warburg, O., On the origin of cancer cells. *Science* **1956**, *123* (3191), 309-314.
- 635 9. Hrubý, M.; Koňák, Č.; Ulbrich, K., Polymeric micellar pH-sensitive drug delivery system  
636 for doxorubicin. *Journal of Controlled Release* **2005**, *103* (1), 137-148.
- 637 10. Fong, W. K.; Negrini, R.; Vallooran, J. J.; Mezzenga, R.; Boyd, B. J., Responsive self-  
638 assembled nanostructured lipid systems for drug delivery and diagnostics. *J Colloid Interface Sci*  
639 **2016**, *484*, 320-339.
- 640 11. Boelsma, E.; van de Vijver, L. P.; Goldbohm, R. A.; Klöpping-Ketelaars, I. A.; Hendriks,  
641 H. F.; Roza, L., Human skin condition and its associations with nutrient concentrations in serum  
642 and diet. *The American journal of clinical nutrition* **2003**, *77* (2), 348-355.

- 643 12. Cederberg, C.; Rohss, K.; Lundborg, P.; Olbe, L., Effect of once daily intravenous and oral  
644 omeprazole on 24-hour intragastric acidity in healthy subjects. *Scand J Gastroenterol* **1993**, *28*  
645 (2), 179-184.
- 646 13. Hu, Y.-B.; Dammer, E. B.; Ren, R.-J.; Wang, G., The endosomal-lysosomal system: from  
647 acidification and cargo sorting to neurodegeneration. *Translational Neurodegeneration* **2015**, *4*  
648 (1), 18.
- 649 14. Sorkin, A.; Von Zastrow, M., Signal transduction and endocytosis: close encounters of  
650 many kinds. *Nat Rev Mol Cell Biol* **2002**, *3* (8), 600-614.
- 651 15. Kocak, G.; Tuncer, C.; Bütün, V., pH-Responsive polymers. *Polymer Chemistry* **2017**, *8*  
652 (1), 144-176.
- 653 16. Deirram, N.; Zhang, C.; Kermaniyan, S. S.; Johnston, A. P. R.; Such, G. K., pH-Responsive  
654 Polymer Nanoparticles for Drug Delivery. *Macromolecular Rapid Communications* **2019**, *40* (10),  
655 1800917.
- 656 17. Mezzenga, R.; Seddon, J. M.; Drummond, C. J.; Boyd, B. J.; Schröder-Turk, G. E.;  
657 Sagalowicz, L., Nature-Inspired Design and Application of Lipidic Lyotropic Liquid Crystals.  
658 *Advanced Materials* **2019**, *31* (35), 1900818.
- 659 18. Tan, A.; Hong, L.; Du, J. D.; Boyd, B. J., Self-Assembled Nanostructured Lipid Systems:  
660 Is There a Link between Structure and Cytotoxicity? *Advanced Science* **2019**, *6* (3), 1801223.
- 661 19. Luzzati, V.; Husson, F., The structure of the liquid-crystalline phasis of lipid-water  
662 systems. *J Cell Biol* **1962**, *12*, 207-219.
- 663 20. Luzzati, V.; Reiss-Husson, F., Structure of the Cubic Phase of Lipid-Water Systems.  
664 *Nature* **1966**, *210* (5043), 1351-1352.
- 665 21. Seddon, J. M., Structure of the inverted hexagonal (HII) phase, and non-lamellar phase  
666 transitions of lipids. *Biochim Biophys Acta* **1990**, *1031* (1), 1-69.
- 667 22. Kaasgaard, T.; Drummond, C. J., Ordered 2-D and 3-D nanostructured amphiphile self-  
668 assembly materials stable in excess solvent. *Physical Chemistry Chemical Physics* **2006**, *8* (43),  
669 4957-4975.
- 670 23. Guillot, S.; Moitzi, C.; Salentinig, S.; Sagalowicz, L.; Leser, M. E.; Glatter, O., Direct and  
671 indirect thermal transitions from hexosomes to emulsified micro-emulsions in oil-loaded  
672 monoglyceride-based particles. *Colloids and Surfaces A: Physicochemical and Engineering*  
673 *Aspects* **2006**, *291* (1), 78-84.
- 674 24. Yaghmur, A.; de Campo, L.; Salentinig, S.; Sagalowicz, L.; Leser, M. E.; Glatter, O., Oil-  
675 loaded monolinolein-based particles with confined inverse discontinuous cubic structure (Fd3m).  
676 *Langmuir* **2006**, *22* (2), 517-521.
- 677 25. Yaghmur, A.; de Campo, L.; Sagalowicz, L.; Leser, M. E.; Glatter, O., Emulsified  
678 microemulsions and oil-containing liquid crystalline phases. *Langmuir* **2005**, *21* (2), 569-577.
- 679 26. Boyd, B. J.; Whittaker, D. V.; Khoo, S.-M.; Davey, G., Lyotropic liquid crystalline phases  
680 formed from glycerate surfactants as sustained release drug delivery systems. *International*  
681 *Journal of Pharmaceutics* **2006**, *309* (1), 218-226.
- 682 27. Phan, S.; Fong, W.-K.; Kirby, N.; Hanley, T.; Boyd, B. J., Evaluating the link between  
683 self-assembled mesophase structure and drug release. *International Journal of Pharmaceutics*  
684 **2011**, *421* (1), 176-182.
- 685 28. Negrini, R.; Mezzenga, R., pH-responsive lyotropic liquid crystals for controlled drug  
686 delivery. *Langmuir* **2011**, *27* (9), 5296-5303.

- 687 29. Negrini, R.; Fong, W.-K.; Boyd, B. J.; Mezzenga, R., pH-responsive lyotropic liquid  
688 crystals and their potential therapeutic role in cancer treatment. *Chemical Communications* **2015**,  
689 *51* (30), 6671-6674.
- 690 30. Oka, T.; Tsuboi, T.-a.; Saiki, T.; Takahashi, T.; Alam, J. M.; Yamazaki, M., Initial Step of  
691 pH-Jump-Induced Lamellar to Bicontinuous Cubic Phase Transition in  
692 Dioleoylphosphatidylserine/Monoolein. *Langmuir* **2014**, *30* (27), 8131-8140.
- 693 31. Salentinig, S.; Sagalowicz, L.; Glatter, O., Self-assembled structures and pKa value of oleic  
694 acid in systems of biological relevance. *Langmuir* **2010**, *26* (14), 11670-11679.
- 695 32. Gontsarik, M.; Mohammadtaheri, M.; Yaghmur, A.; Salentinig, S., pH-Triggered  
696 nanostructural transformations in antimicrobial peptide/oleic acid self-assemblies. *Biomater Sci*  
697 **2018**, *6* (4), 803-812.
- 698 33. Fong, C.; Zhai, J.; Drummond, C. J.; Tran, N., Micellar Fd3m cubosomes from monoolein  
699 – long chain unsaturated fatty acid mixtures: Stability on temperature and pH response. *Journal of*  
700 *Colloid and Interface Science* **2020**, *566*, 98-106.
- 701 34. Kulkarni, C. V.; Tang, T.-Y.; Seddon, A. M.; Seddon, J. M.; Ces, O.; Templer, R. H.,  
702 Engineering bicontinuous cubic structures at the nanoscale—the role of chain splay. *Soft Matter*  
703 **2010**, *6* (14), 3191-3194.
- 704 35. Briggs, J.; Chung, H.; Caffrey, M., The Temperature-Composition Phase Diagram and  
705 Mesophase Structure Characterization of Monoolein/Water System. *Journal de Physique II* **1996**,  
706 *6* (5), 723-751.
- 707 36. Walsh, C. L.; Nguyen, J.; Szoka, F. C., Synthesis and characterization of novel zwitterionic  
708 lipids with pH-responsive biophysical properties. *Chemical Communications* **2012**, *48* (45), 5575-  
709 5577.
- 710 37. Nakano, M.; Teshigawara, T.; Sugita, A.; Leesajakul, W.; Taniguchi, A.; Kamo, T.;  
711 Matsuoka, H.; Handa, T., Dispersions of Liquid Crystalline Phases of the Monoolein/Oleic  
712 Acid/Pluronic F127 System. *Langmuir* **2002**, *18* (24), 9283-9288.
- 713 38. Kollmitzer, B.; Heftberger, P.; Rappolt, M.; Pabst, G., Monolayer spontaneous curvature  
714 of raft-forming membrane lipids. *Soft Matter* **2013**, *9* (45), 10877-10884.
- 715 39. Tyler, A. I.; Barriga, H. M.; Parsons, E. S.; McCarthy, N. L.; Ces, O.; Law, R. V.; Seddon,  
716 J. M.; Brooks, N. J., Electrostatic swelling of bicontinuous cubic lipid phases. *Soft Matter* **2015**,  
717 *11* (16), 3279-3286.
- 718 40. Caboi, F.; Amico, G. S.; Pitzalis, P.; Monduzzi, M.; Nylander, T.; Larsson, K., Addition  
719 of hydrophilic and lipophilic compounds of biological relevance to the monoolein/water system.  
720 I. Phase behavior. *Chemistry and Physics of Lipids* **2001**, *109* (1), 47-62.
- 721 41. Dong, Y.-D.; Tilley, A. J.; Larson, I.; Lawrence, M. J.; Amenitsch, H.; Rappolt, M.;  
722 Hanley, T.; Boyd, B. J., Nonequilibrium Effects in Self-Assembled Mesophase Materials:  
723 Unexpected Supercooling Effects for Cubosomes and Hexosomes. *Langmuir* **2010**, *26* (11), 9000-  
724 9010.
- 725 42. Tyler, A. I.; Shearman, G. C.; Brooks, N. J.; Delacroix, H.; Law, R. V.; Templer, R. H.;  
726 Ces, O.; Seddon, J. M., Hydrostatic pressure effects on a hydrated lipid inverse micellar Fd3m  
727 cubic phase. *Phys Chem Chem Phys* **2011**, *13* (8), 3033-3038.
- 728 43. Boyd, B. J.; Rizwan, S. B.; Dong, Y.-D.; Hook, S.; Rades, T., Self-Assembled Geometric  
729 Liquid-Crystalline Nanoparticles Imaged in Three Dimensions: Hexosomes Are Not Necessarily  
730 Flat Hexagonal Prisms. *Langmuir* **2007**, *23* (25), 12461-12464.

- 731 44. Sagalowicz, L.; Acquistapace, S.; Watzke, H. J.; Michel, M., Study of Liquid Crystal Space  
732 Groups Using Controlled Tilting with Cryogenic Transmission Electron Microscopy. *Langmuir*  
733 **2007**, *23* (24), 12003-12009.
- 734 45. Barauskas, J.; Johnsson, M.; Tiberg, F., Self-assembled lipid superstructures: beyond  
735 vesicles and liposomes. *Nano Lett* **2005**, *5* (8), 1615-1619.
- 736 46. Demurtas, D.; Guichard, P.; Martiel, I.; Mezzenga, R.; Hebert, C.; Sagalowicz, L., Direct  
737 visualization of dispersed lipid bicontinuous cubic phases by cryo-electron tomography. *Nat*  
738 *Commun* **2015**, *6*, 8915.
- 739 47. Duesing, P. M.; Templer, R. H.; Seddon, J. M., Quantifying Packing Frustration Energy in  
740 Inverse Lyotropic Mesophases. *Langmuir* **1997**, *13* (2), 351-359.
- 741 48. Basham, M.; Filik, J.; Wharmby, M. T.; Chang, P. C.; El Kassaby, B.; Gerring, M.;  
742 Aishima, J.; Levik, K.; Pulford, B. C.; Sikharulidze, I.; Sneddon, D.; Webber, M.; Dhesi, S. S.;  
743 Maccherozzi, F.; Svensson, O.; Brockhauser, S.; Naray, G.; Ashton, A. W., Data Analysis  
744 WorkbeNch (DAWN). *J Synchrotron Radiat* **2015**, *22* (3), 853-858.
- 745 49. Filik, J.; Ashton, A. W.; Chang, P. C. Y.; Chater, P. A.; Day, S. J.; Drakopoulos, M.;  
746 Gerring, M. W.; Hart, M. L.; Magdysyuk, O. V.; Michalik, S.; Smith, A.; Tang, C. C.; Terrill, N.  
747 J.; Wharmby, M. T.; Wilhelm, H., Processing two-dimensional X-ray diffraction and small-angle  
748 scattering data in DAWN 2. *Journal of applied crystallography* **2017**, *50* (Pt 3), 959-966.
- 749 50. Schindelin, J.; Arganda-Carreras, I.; Frise, E.; Kaynig, V.; Longair, M.; Pietzsch, T.;  
750 Preibisch, S.; Rueden, C.; Saalfeld, S.; Schmid, B.; Tinevez, J. Y.; White, D. J.; Hartenstein, V.;  
751 Eliceiri, K.; Tomancak, P.; Cardona, A., Fiji: an open-source platform for biological-image  
752 analysis. *Nat Methods* **2012**, *9* (7), 676-682.
- 753 51. Tinevez, J. Y.; Perry, N.; Schindelin, J.; Hoopes, G. M.; Reynolds, G. D.; Laplantine, E.;  
754 Bednarek, S. Y.; Shorte, S. L.; Eliceiri, K. W., TrackMate: An open and extensible platform for  
755 single-particle tracking. *Methods* **2017**, *115*, 80-90.

756